



Leading-edge vortex dynamics and impulse-based lift force analysis of oscillating airfoils

Firas F. Siala¹ · James A. Liburdy¹

Received: 25 April 2019 / Revised: 6 August 2019 / Accepted: 17 August 2019 / Published online: 21 September 2019
© Springer-Verlag GmbH Germany, part of Springer Nature 2019

Abstract

The vortex dynamics and lift force generated by a sinusoidally heaving and pitching airfoil during dynamic stall are experimentally investigated for reduced frequencies of $k = fc/U_\infty = 0.06\text{--}0.16$, pitching amplitude of $\theta_0 = 75^\circ$ and heaving amplitude of $h_0/c = 0.6$. The lift force is calculated from the velocity fields using the finite-domain impulse theory. The concept of moment-arm dilemma associated with the impulse equation is revisited to shed light on its physical impact on the calculated forces. It is shown that by selecting an objectively defined origin of the moment-arm, the impulse force equation can be greatly simplified to two terms that have a clear physical meaning: (1) the time rate of change of impulse of vortical structures within the control volume and (2) Lamb vector that indirectly captures the contribution of vortical structures outside of the control volume. The results show that the trend of the lift force is dependent on the formation of the leading-edge vortex, as well as its time rate of change of circulation and chord-wise advection relative to the airfoil. Additionally, the trailing-edge vortex, which is observed to only form for $k \leq 0.10$, is shown to have lift-diminishing effects that intensify with increasing reduced frequency. Lastly, the concept of optimal vortex formation is investigated. The leading-edge vortex is shown to attain the optimal formation number of approximately 4 for $k \leq 0.1$, when the scaling is based on the leading-edge shear velocity. For larger values of k the vortex growth is delayed to later in the cycle and does not reach its optimal value. The result is that the peak lift force occurs later in the cycle. This has consequences on power production which relies on correlation of the relative timing of lift force and heaving velocity.

1 Introduction

Flow physics of oscillating surfaces has become a very important area of study for a wide range of applications, such as the development of micro-air vehicles and energy-harvesting devices (Tuncer and Platzer 2000; Zhu 2011; Mackowski and Williamson 2015; Siala and Liburdy 2015). A large contribution to the existing knowledge has come through the studies of flapping flight of insects, birds and bats (Leishman 1994; Ellington et al. 1996; Ellington 1999; Madangopal et al. 2005; Platzer et al. 2008; Hubel et al. 2009). The oscillatory/flapping kinematics of these natural fliers may exploit several lift-enhancing mechanisms such as dynamic stall and vortex-wake recapture, among others (Srygley and Thomas 2002). A common model of oscillatory flight is the combined heaving and pitching motion of

an airfoil at large angles of attack, in which the formation and shedding of leading-edge vortices (LEVs) exhibit a large impact on the flow behaviour and instantaneous aerodynamic forces (Hubel and Tropea 2010; Moriche et al. 2017). Although the general role of LEVs is well understood; they produce regions of low pressure on the suction side of the airfoil to generate a large suction force, yet developing fundamental theories that can predict their effects on the transient aerodynamic forces remains to be quite challenging to the aerodynamics community.

Classical unsteady theories of aerodynamics, the most prevalent of which are the models of Wagner (1925) and Theodorsen (1934), have been used extensively with success in problems related to aeroelasticity and fluttering. However, since these models are based on potential flow theory, they do not capture the effects of separated flow and LEVs, thereby limiting their application to small amplitude kinematics where the boundary-layer remains attached throughout the unsteady motion. In recent years, more advanced models based on discrete-vortex methods have been employed to model unsteady flows during dynamic stall (Xia and Mohseni 2013; Hammer

✉ James A. Liburdy
liburdyj@oregonstate.edu

¹ Mechanical Engineering, Oregon State University, Corvallis, OR 97331, USA

et al. 2014; Liu et al. 2016; Darakananda et al. 2016). In these methods, potential-flow theory is modified to include discrete point vortices to represent free vortical structures and shear layers. Typically, the trajectory of these point vortices is determined by the Kirchhoff velocity (Darakananda et al. 2016) or Brown–Michael equation (Brown 1954). However, such models are based on some ad-hoc criteria for LEV inception and shedding. For example, the LEV strength must reach an extremum before it is allowed to evolve as a simple point vortex using the Brown–Michael equation. Furthermore, Ramesh et al. (2014) developed the leading-edge suction parameter (LESP), which is equivalent to the first Fourier coefficient (A_0) in unsteady thin airfoil theory, to predict the onset of LEV formation. This method requires calibration using highly resolved simulations to determine a critical LESP value, at which the flow begins to separate from the leading edge. They show that the critical LESP value they determined is universal for a given airfoil geometry and Reynolds number. Once the LEV is formed, its evolution is determined using inviscid flow theory. While this method provides reasonable estimates of aerodynamic force coefficients, it still requires high-cost simulations to pre-determine the onset of flow separation. In addition, the exact contribution of LEVs and other free vortices is not explicitly highlighted, which makes it difficult to develop fundamental theories of vortex dynamics and their role in aerodynamic force production.

One promising tool for computing the fluid dynamic forces is based on the concept of hydrodynamic impulse (Lin and Rockwell 1996; Epps 2010; Kim et al. 2013). Originally, the impulse concept was introduced to bypass the integration of total momentum which is not well defined in an infinite region, since in general the momentum integral is only conditionally convergent (Lamb 1932; Lighthill 1986; Saffman 1992; Batchelor 2000). The impulse-based force equation for an unsteady moving body in unbounded, incompressible flow can be written as follows:

$$\mathbf{F} = -\frac{\rho}{N-1} \frac{d}{dt} \int_{V_\infty} (\mathbf{x} - \mathbf{x}_0) \times \boldsymbol{\omega} dV + \frac{\rho}{1-N} \frac{d}{dt} \oint_{S_B} (\mathbf{x} - \mathbf{x}_0) \times (\mathbf{n} \times \mathbf{u}) dS \tag{1}$$

where ρ is fluid density, \mathbf{x} is the position vector, \mathbf{x}_0 is the origin location of the position vector, $\boldsymbol{\omega}$ is the vorticity vector, \mathbf{u} is the velocity vector, \mathbf{n} is the normal unit vector and $N = \nabla \cdot \mathbf{x}$ is the dimension of space. The details of the control volume used for the application of Eq. (1) are given in Fig. 1. The first term is evaluated over the entire flow field (V_∞) and represents the rate of change of flow impulse. The second term is evaluated over the body surface (S_B) and it represents the inertial force of the fluidic body. One particular constraint with this formulation is that the entire vorticity field must be captured in the control volume (V_∞).

Practically, this limits its use to the early times of impulsively-started flows, where the entire vorticity field remains inside the control volume.

The use of impulse theory has also gained popularity in constructing semi-empirical low-order models. For example Babinsky et al. (2016) and Stevens and Babinsky (2017) have applied a linearized version of the impulse formulation (Kármán 1938) to experimental data to model the transient lift force of impulsively pitching and surging airfoils. They decomposed the rate of change of impulse into two terms: vortex circulation growth and vortex advection, where both terms are calculated empirically from experimental data. They show that the total lift force at the beginning of the motion is primarily dictated by the LEV growth. Once the LEV stops growing, the LEV advection relative to the trailing-edge vortex (TEV) becomes more dominant. Overall, they obtain reasonable lift force estimates by assuming that all relevant vorticity is contained within the LEV and TEV. Furthermore, Wang and Eldredge (2013) used the impulse-matching approach (Tchieu and Leonard 2011) in conjunction with discrete-vortex methods to model the effects of LEVs on impulsively started flat plates at various angles of attacks. The impulse-matching approach is used as an alternative to the Brown–Michael equation to relax the vortex shedding criterion required by the latter method. One limitation associated with this approach that the authors address is the use of the Kutta condition to determine the vortex strength as a function of time. They suggest that calculating the vortex strength empirically might improve the accuracy of their model. Ideally, one may develop universal scaling laws of vortex dynamics for a wide range of operational parameters that can be used as inputs in such models. For example, the idea of optimal vortex formation number (Dabiri 2009) could potentially serve as a unifying principle in constructing low-order models under the proper conditions. Onoue and Breuer (2016) investigated the LEV formation number of pitching airfoils for a wide range of amplitudes,

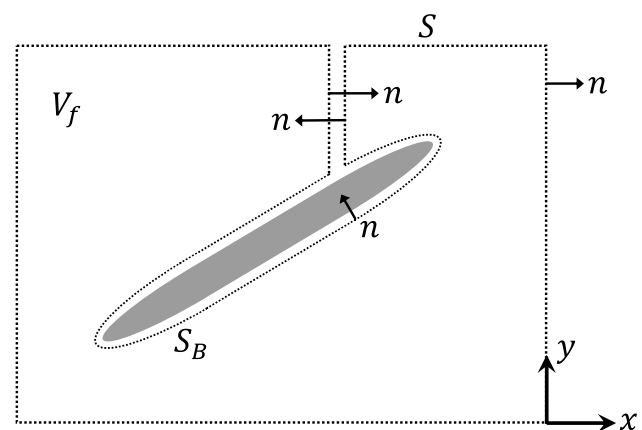


Fig. 1 Domain of integration for the evaluation of aerodynamic forces on an airfoil

reduced frequencies and Reynolds numbers. They show that the time-history of LEV circulation growth collapses on a single curve, where the maximum formation number was found to approximately equal to 4, agreeing remarkably well with the theory (Gharib et al. 1998).

Noca (1997) has expanded on the impulse theory and derived the force equation for arbitrary finite domains using the derivative moment transformation (DMT) identity (Wu et al. 2007). The force equation is written as follows:

$$\begin{aligned} \mathbf{F} = & -\frac{\rho}{N-1} \frac{d}{dt} \int_{V_f} (\mathbf{x} - \mathbf{x}_0) \times \boldsymbol{\omega} dV \\ & + \rho \oint_S \mathbf{n} \cdot \left(\frac{1}{2} u^2 \mathbf{I} - \mathbf{u} \otimes \mathbf{u} \right) dS + \oint_S \mathbf{n} \cdot \lambda_{\text{imp}} dS \quad (2) \\ & + \frac{1}{N-1} \rho \frac{d}{dt} \oint_{S_B} (\mathbf{x} - \mathbf{x}_0) \times (\mathbf{n} \times \mathbf{u}) dS \end{aligned}$$

where V_f is the fluidic volume, S is the exterior surface of the control volume and S_B is the airfoil surface. The term λ_{imp} may be written as follows:

$$\begin{aligned} \lambda_{\text{imp}} = & \frac{\rho}{N-1} \boldsymbol{\omega} ((\mathbf{x} - \mathbf{x}_0) \times \mathbf{u}) - \frac{\rho}{N-1} [\mathbf{u} \otimes ((\mathbf{x} - \mathbf{x}_0) \times \boldsymbol{\omega})] + \mathbf{T} \\ & + \frac{1}{N-1} [(\mathbf{x} - \mathbf{x}_0) \cdot (\nabla \cdot \mathbf{T}) \mathbf{I} - (\mathbf{x} - \mathbf{x}_0) \otimes (\nabla \cdot \mathbf{T})] \quad (3) \end{aligned}$$

where \mathbf{I} and \mathbf{T} represent the identity and viscous stress tensors, respectively. Unsteady force evaluation based on the finite-domain impulse theory has attracted wide attention among the experimental fluid dynamics community, as it is often not feasible to directly measure the aerodynamic forces on moving airfoils due to challenges in separating the inertial contributions (Rival et al. 2009). This is especially problematic in wind tunnel experiments, where the density of the airfoil can be orders of magnitude greater than the density of air (Totpal 2017). Other force estimation techniques based on the integral momentum approach requires the evaluation of the pressure field which can be a non-trivial task in experimental fluid dynamics (Van Oudheusden 2013). Although many researchers have successfully computed the pressure field and obtained reasonable force estimates (Liu and Katz 2006; Charonko et al. 2010; Dabiri et al. 2014; Villegas and Diez 2014), these methods provide a global force estimation, where the contributions of the local vortical structures are hidden. Several authors applied Eq. (2), or other forms of it, to experimental (Noca 1997; Baik et al. 2011; DeVoria et al. 2014; Siala et al. 2018) and numerical (Li and Lu 2012; Mohebbian and Rival 2012; Kang et al. 2018) data to calculate the unsteady lift force. The impulse approach offers various distinct advantages. First, it does not require the evaluation of the pressure field, which is very practical for experiments based on particle image velocimetry

(PIV). Second, the force can be easily decomposed into circulatory and non-circulatory contributions, which provides useful insights of the physical mechanisms responsible for force generation. In fact, this decomposition is similar to that found in Theodorsen’s model (Theodorsen 1934), except that it also includes the effects of free vortices. Third, and perhaps most importantly, the impulse-based force equation is linearly dependent on vorticity, which means that the total impulse in the flow field can be treated as a superposition of impulses of every individual vortex structure in the flow. Note that the impulse of each vortex structure, which is ultimately determined by the motion of the vortex, is dependent on all of the other vorticity in the fluid through their Biot–Savart influences on the velocity of the vortex. These advantages provide the impulse approach with great utility for theoretical modeling of unsteady airfoils exhibiting dynamic stall, as it is easier to describe these flows in terms of vorticity.

One particular challenge with Eq. (2) is that it contains cumbersome boundary integral terms with ambiguous physical meanings, which makes it difficult to identify the mechanisms responsible for the lift production and to construct low-order models. Kang et al. (2018) proposed using the minimum-domain impulse theory, which greatly simplifies Eq. (2) by dropping many of the surface integral terms. The requirement for using their theory is that the control volume must not cut through regions of significant vorticity. They follow the idea of Flood Fill (Torbert 2016) to choose a different control volume at each instant in time to find a critical vorticity threshold under which the minimum-domain theory is valid. While this method is effective, it may be difficult to experimentally pursue, since one is highly limited by the field of view provided by the PIV imaging system.

In the pursuit of relaxing the criterion of the minimum-domain theory of Kang et al. (2018), we provide in this paper an alternative approach to significantly reduce the finite-domain, impulse-based force equation. The reduced-order impulse formulation is then used to provide insight into transient lift force production mechanisms of a heaving and pitching airfoil at very large amplitudes of motion. We are specifically interested in operating at relatively low reduced frequencies associated with flow energy harvesting applications (Zhu 2011), where there is a dearth of knowledge concerning the evolution of LEV strength, size and trajectory. The flow field around the heaving and pitching airfoil is obtained experimentally using two-component PIV measurements. The results of this work will aid in constructing low-order models of the aerodynamic forces generated during dynamic stall for continuously oscillating/flapping airfoils (as opposed to impulsively started flows).

2 Methodology

2.1 Experimental setup

Experiments were conducted in a closed-loop wind tunnel (1.37×1.52 m) with turbulence intensities below 2%. The airfoil used in this study was manufactured in-house using fused deposition modeling and has a chord length, thickness and aspect ratio of 125 mm, 6.25 mm and 2, respectively. The airfoil is a flat plate and has elliptic leading and trailing-edge tips with 5:1 major to minor axis ratio. Stationary end plates were placed approximately 2 mm away from the side-edges to suppress the formation of tip vortices and to simulate two dimensional flow conditions. The airfoil is attached to a motion device using a titanium rod spanning through the mid-chord of the airfoil. The motion device is used to generate the heaving and pitching motion of the airfoil according to the following equations:

$$h(t) = h_0 \cos(2\pi ft) \quad (4)$$

$$\theta(t) = \theta_0 \cos(2\pi ft + \Phi) \quad (5)$$

where h_0 is the heaving amplitude, f the oscillation frequency, θ_0 the pitching amplitude, Φ the phase shift between heaving and pitching and t is time. Heaving was achieved using a scotch-yoke mechanism and the pitching motion used a combination of a scotch-yoke mechanism and a rack and pinion arrangement. The motion device was controlled using a LabVIEW program. The airfoil motion was verified by recording a video of the oscillatory motion, which was then used to calculate the heaving and pitching motion using an object-tracking software (Totpal 2017). The root mean

square error of the heaving and pitching motion was found to be less than 1% of the heaving and pitching amplitudes, respectively. The experimental setup in the wind tunnel and the motion device are sketched in Fig. 2.

Two-component, phase-locked PIV measurements were collected using a dual-head Nd:YAG-pulsed laser (Ever-Green, 145 mJ/pulse, max repetition rate of 15 Hz) operating at the 532 nm wavelength. A light sheet of approximately 1.5 mm thickness was generated at the mid-span of the airfoil using a LaVision optics module. An in-house designed Laskin nozzle atomizer provided the seeding particles using vegetable oil. Particle images were collected using a CCD camera (Image Pro, LaVision) with a resolution of 1600×1200 pixels. The camera was equipped with a 50 mm focal length lens and a band-pass filter centered at 532 nm. The PIV system was configured to obtain a vector field resolution of 1.8 mm (approximately 70 vectors per chord length). PIV images were processed with DaVis v8.4 software. Particle position displacements were determined using a cross-correlation method on sequential images. The calculations were conducted on two passes of interrogation window size of 64×64 pixels, followed by two passes of interrogation window size of 32×32 pixels, where a 50% overlap was used. A high-accuracy sub-pixel peak-fitting algorithm specific to DaVis[®] software was used for the final passes. The time between pulses was set such that an average of 8 pixel displacement per interrogation window was achieved in the streamwise direction. Minimum peak validation of 1.2 (ratio of the highest to second highest correlation peaks) and moving-average validation schemes were used to reject outliers, with a vector rejection rate of less than 2%.

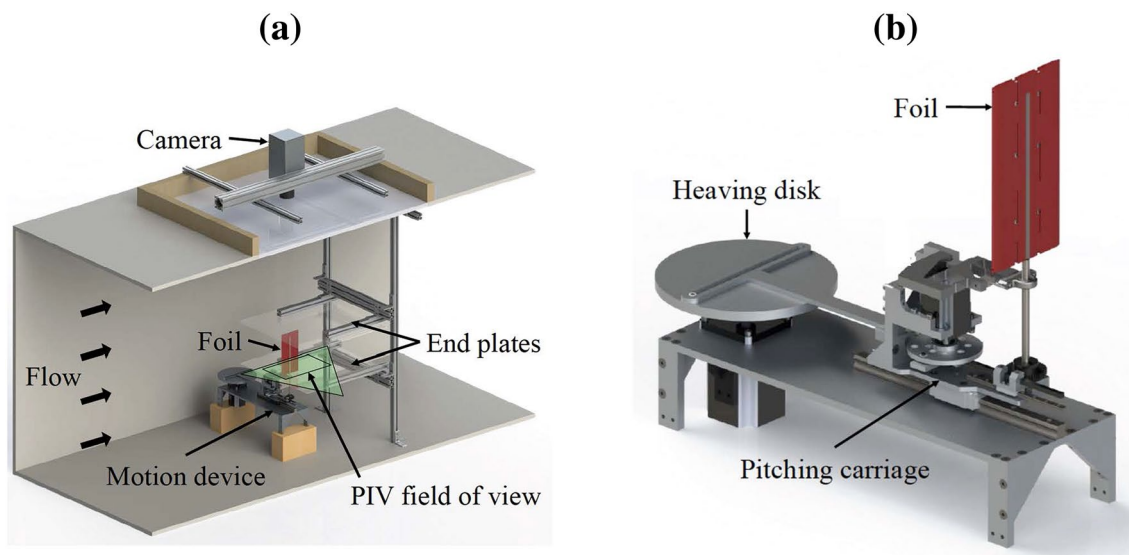


Fig. 2 **a** Drawing of the experimental setup illustrating the motion device, airfoil orientation and optical system and **b** zoomed-in view of the motion device. Figures are adopted from Totpal (2017)

The phase-locked velocity fields were calculated by averaging one hundred images at each phase of interest. A total of 116 phases throughout the downstroke motion with an equal spacing of $\Delta t/T = 0.004$ (where T is the oscillation period) were acquired. The PIV system and airfoil motion were synchronized using LabVIEW. The motion device was run for at least 5 minutes prior to collecting PIV measurements to eliminate any initial transient effects.

The use of Eq. (2) to calculate the aerodynamic forces requires capturing the entire flow field surrounding the airfoil. To obtain data in the shadow region caused by the laser illumination, the experiments were repeated at a phase delay of 180° for each phase of interest. The 180° out of phase flow fields were then mirrored and stitched to the rest of the vector field to construct the full flow field surrounding the airfoil. This can be done because the flow, airfoil shape and motion are all symmetric. A similar approach was used by Lua et al. (2015). Additionally, a second camera was used to capture the flow field in the downstream region. The two cameras were overlapped by 14 vectors and the overlapped region was smoothed with a 3×3 moving-average filter.

2.2 Uncertainty quantification

The particle displacement uncertainty was calculated using the statistical correlation technique developed by Wieneke (2015). Note that this method only estimates the random errors that are associated with camera noise, particle focus and out-of-plane motion, among others (Willert and Gharib 1991), whereas the systematic errors that are typically influenced by the calibration errors and peak-locking effects are not taken into account. For calibration, we use the pinhole fitting model, and the root mean square of the fit is 0.33 pixels. The peak-locking effect was avoided using particle image size of approximately 2.1 pixels (estimated from the peak width of the autocorrelation peak of a typical particle image), which is greater than the minimum size of 1 pixel (Wieneke 2015). The particle displacement uncertainty was then propagated to velocity and vorticity calculations using the technique provided by Sciacchitano and Wieneke (2016). Finally, the uncertainty was propagated to estimate the uncertainty in the lift force. The maximum and mean uncertainties of the velocity components, span-wise vorticity and aerodynamic lift force are listed in Table 1 as a percentage of their respective maximum values. We also include uncertainty of free stream velocity measured in the wind tunnel without the airfoil and motion device. All uncertainties are reported using a 95% confidence interval.

As pointed out in the previous section, one of the main motivations of this work is the need for an alternative tool to estimate the transient aerodynamics forces, since direct force measurement of high-amplitude oscillating airfoils operating in wind tunnels is usually unfeasible. Unsteady

Table 1 Maximum and mean uncertainty of free stream velocity, velocity components, span-wise vorticity and aerodynamic lift force at $k = 0.16$

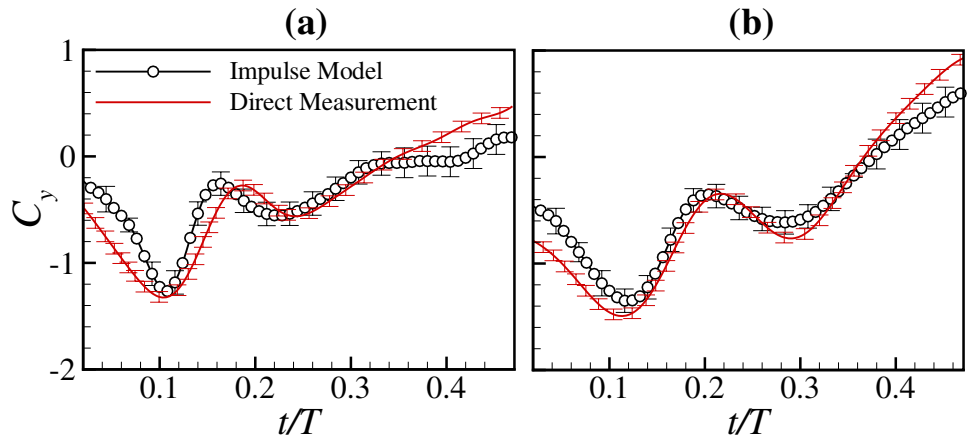
Variable	Maximum uncertainty (%)	Mean uncertainty (%)
U_∞	0.3	0.2
u	3.5	1.3
v	5.8	2.1
w_z	9.1	4.7
F_y	13.6	8.2

All uncertainties are reported using a 95% confidence interval

aerodynamic flows indicate that the time scale of airfoil motion is smaller than the time scale of the flow, where the degree of unsteadiness is often described by the reduced frequency ($k = fc/U_\infty$). The difficulty in measuring transient forces of highly unsteady airfoils is due to the inertial forces growing rapidly at high oscillation frequencies (proportional to f^2), whereas the aerodynamic forces grow with U_∞^2 . In fact, when $k > 0.08$, the inertial forces become at least an order-of-magnitude larger than the aerodynamic forces, and therefore the accuracy of the force measurements becomes unreliable. For this reason in this study, accurate direct force measurements for $k > 0.08$ are not presented.

In Fig. 3, the transient lift force coefficient ($C_y = 2F_y/\rho U_\infty^2 c$) obtained from the impulse formulation is compared with the results obtained from direct force measurements during the downstroke motion at $k = 0.06$ and $k = 0.08$. Note that the transient forces are shown only from $t/T = 0.02$ to $t/T = 0.48$, as we were unable to obtain consistent impulse-based force measurements at these times due to unreliable curve-fitting of the raw data prior to taking the time derivative of the impulse term (first term of Eq. (2)). It is shown that the force magnitude and trend are well captured by the impulse formulation. The largest discrepancy occurs at the beginning of the downstroke, where the flow remains fully attached to the airfoil surface. Here, the force generation is dominated by the bound vorticity, which is not well resolved by the PIV experiments, and as a consequence, the impulse-based formulation under-predicts the force. Once the flow at the leading edge separates and forms an LEV, the impulse formulation and direct force measurement are in excellent agreement. At this point, it is expected that the contribution of surface vorticity to the lift force becomes negligible (Morange et al. 2017). The explanation for this has been provided by Ford and Babinsky (2013), who have shown that the bound circulation (due to surface vorticity) of unsteady airfoils at large angles of attack tends toward zero and the LEV circulation is nearly equal and opposite to the circulation shed from the trailing edge. For the motion kinematics used in this study, the flow is observed to be attached

Fig. 3 Comparison of the transient lift coefficient obtained from the impulse formulation with the results obtained from direct force measurements at **a** $k = 0.06$ and **b** $k = 0.08$; results are given for the half cycle beginning when the foil is at the top heaving position



to the airfoil surface for only a relatively short period of time, thus providing validity in the use of impulse formation.

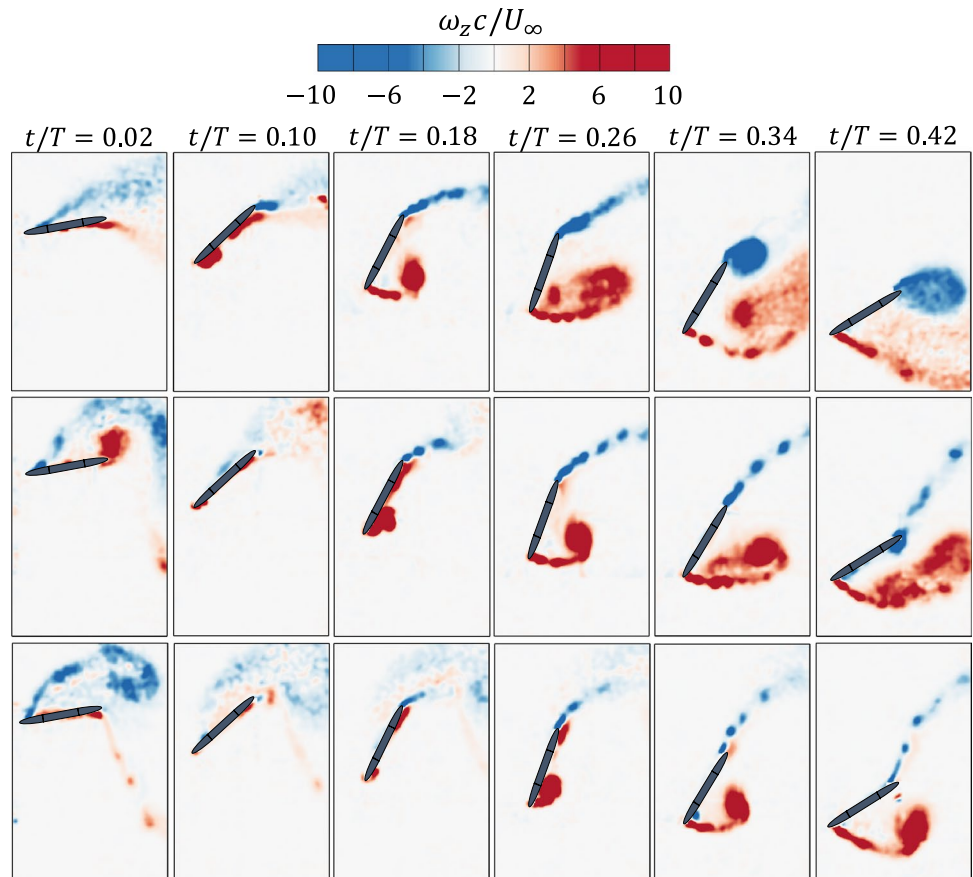
3 Results

In this section, we present results for reduced frequencies of $k = 0.06 - 0.16$, while holding the heaving amplitude, pitching amplitude, phase shift and pitching axis fixed at $h_0/c = 0.6$, $\theta_0 = 75^\circ$, $\Phi = 90^\circ$ and $x_p/c = 0$ (mid-chord),

respectively. The reduced frequency was varied by changing the free stream velocity, resulting in Reynolds numbers ($Re = U_\infty c/\nu$, where ν is the kinematic viscosity) ranging from 7,216 to 16,889 for $k = 0.16$ and $k = 0.06$, respectively. These parameters have been shown to produce high energy harvesting efficiencies (Zhu 2011). Due to the symmetry of the problem, the results are only provided for the downstroke motion of the airfoil.

Figure 4 shows the non-dimensional spanwise vorticity evolution for $k = 0.06, 0.10$ and 0.14 . The flow approaches

Fig. 4 Vorticity field for discrete phases during the downstroke. Top row: $k = 0.06$, middle row: $k = 0.10$ and bottom row: $k = 0.14$



from the left-hand side and the non-dimensional time $t/T = 0$ corresponds to the top heaving position and $t/T = 0.5$ is the bottom heaving position. For $k = 0.06$, the leading-edge shear layer on the top surface of the airfoil is shown to be separated due to the LEV shedding during the upstroke motion. Once the angle of attack is large enough (in the negative direction), the shear layer becomes attached to the top surface, while it begins to separate and roll-up into an LEV on the bottom surface at $t/T \approx 0.10$. The shear layer feeds the LEV with vorticity, which results in the increase of LEV strength and size over time. By the time the LEV grows past the trailing edge ($t/T \approx 0.26$), the trailing-edge shear layer begins to roll-up into a trailing-edge vortex (TEV). Eventually, the LEV and TEV both shed into the wake to form a Karman-like vortex street (i.e. drag producing wake). For $t/T > 0.42$, the flow over the airfoil is completely separated and full stall is attained.

Early in the cycle for $k = 0.10$, it is shown that a coherent positive vortical structure is shed from the trailing edge. This corresponds to the TEV formed during the upstroke. Since the convective time scale of the flow for high reduced frequencies is relatively larger than for lower reduced frequencies, the formation and advection of flow structures occur at a slower rate for $k = 0.10$ when compared to $k = 0.06$. The leading-edge shear layer separates and rolls into an LEV at $t/T \approx 0.18$. The TEV begins to form at $t/T \approx 0.42$, however, its size is significantly smaller than for $k = 0.06$.

For $k = 0.14$, at early times a large negative vortex structure is observed in the near wake of the airfoil. This is the LEV that was shed during the upstroke. The convective time scale at this reduced frequency is significantly larger than the airfoil oscillation time scale, thereby enabling the airfoil at the beginning of downstroke to capture the LEV from the upstroke. Similarly to $k = 0.06$ and 0.10 , the shear layer from the bottom surface eventually rolls into an LEV ($t/T \approx 0.260$). Furthermore, it is shown that by the time the LEV approaches the trailing edge, the airfoil is already at a relatively small geometric angle of attack and so the trailing edge shear layer is not strong enough to roll-up into a TEV.

The conclusions of the above discussion are as follows: first, the inception of the LEV is delayed in time for larger reduced frequencies. As the reduced frequency increases, the time scale of the airfoil motion becomes smaller relative to the flow time scale. This means that the shear layer takes a longer time to react to the change of angle of attack when k is larger, thus delaying flow separation. Second, the growth rate of the LEV decreases with increasing reduced frequency. This is the result of the decrease of the feeding shear layer velocity at higher reduced frequencies. This is explained as follows. The shear layer velocity can be approximated as the vector sum of the local velocity of the leading edge and the component of the free stream in the direction of the airfoil motion (Onoue and Breuer 2016):

$$U_{SL} = U_{\infty} \sin(\theta) - \dot{h} \cos(\theta) - \frac{\dot{\theta} c}{2} \tag{6}$$

where \dot{h} and $\dot{\theta}$ represent the heaving and angular pitching velocities, respectively. As the reduced frequency increases (by either decreasing the free stream velocity or by increasing the oscillation frequency), the shear layer velocity decreases. Lastly, when k is less than 0.12, the trailing-edge shear layer rolls into a TEV. Siala et al. (2017) have shown that when the LEV reaches the trailing edge, a saddle point is created downstream of the airfoil trailing edge, which forces the trailing shear layer to roll-up into a TEV. This phenomena was also reported by Rival et al. (2014) and Widmann and Tropea (2015).

3.1 Leading-edge vortex dynamics

In this section the LEV spatio-temporal dynamics are evaluated which will aid in understanding the mechanisms responsible for the lift force production. The LEV circulation and its trajectory are computed based on the vortex identification technique proposed by Graftieaux et al. (2001). In this method, two scalar functions Γ_1 and Γ_2 derived from the velocity vector field, are used to identify the vortex core location and its boundary, respectively, and are given by:

$$\Gamma_1(p) = \frac{1}{N} \sum_{i=1}^N \frac{((\mathbf{x}_p - \mathbf{x}_i) \times \mathbf{u}_i) \cdot \hat{\mathbf{z}}}{\|\mathbf{x}_p - \mathbf{x}_i\| \cdot \|\mathbf{u}_i\|} \tag{7}$$

$$\Gamma_2(p) = \frac{1}{N} \sum_{i=1}^N \frac{((\mathbf{x}_p - \mathbf{x}_i) \times (\mathbf{u}_i - \bar{\mathbf{u}}_p)) \cdot \hat{\mathbf{z}}}{\|\mathbf{x}_p - \mathbf{x}_i\| \cdot \|\mathbf{u}_i - \bar{\mathbf{u}}_p\|} \tag{8}$$

Subscript i denotes any point in the flow field, \mathbf{x}_p is the position vector, $\hat{\mathbf{z}}$ is the unit vector in the z direction, N is the total number of points in a subregion and $\bar{\mathbf{u}}_p$ is the average velocity evaluated in a sub-region. We evaluate Γ_1 and Γ_2 at every point in the flow field using a 3×3 sub-region ($N = 9$). The vortex core is identified by $|\Gamma_1| \geq 0.9$ and the vortex boundary is characterized by $|\Gamma_2| \geq 2/\pi$ (Graftieaux et al. 2001). Overall, this procedure has been found to provide reliable and reproducible definitions of vortex structures (Morse and Liburdy 2009; Baik et al. 2012; Dunne and McKeon 2015). The LEV circulation is then calculated by integrating the vorticity enclosed by the contour $|\Gamma_2| = 2/\pi$. To calculate the LEV trajectory, the measured velocity vector field is rotated and translated at each instant in time according to the airfoil kinematics given in Eqs. (4) and (5). This is done so that the LEV trajectory is calculated in the frame of reference of the airfoil. Then, the location of the largest value of Γ_1 (on the condition that it is greater

than 0.9) is tracked for the entire time until the LEV begins to leave the control volume.

In Fig. 5a the LEV circulation normalized by the average shear layer velocity and chord length is plotted versus t/T for all reduced frequencies. In general, once the LEV is formed, it entrains vorticity from the feeding shear layer and the circulation grows at a rate proportional to U_{SL}^2 (Eldredge and Jones 2019). It is worthwhile to mention that this non-dimensionalization of LEV circulation is analogous to the optimal vortex formation number given by Dabiri (2009). This concept is based on the argument that for a vortex generator with a given length scale and feeding shear layer velocity, the maximum possible vortex formation number is approximately equal to 4. Here, the airfoil can be thought of as a vortex generator with a length scale c and average feeding shear layer velocity \bar{U}_{SL} . It is shown that for $k \leq 0.10$, the maximum circulation is approximately 3.8–4. In this case, the shear layer feeds the LEV with vorticity until the LEV grows to the size of airfoil chord length (Fig. 5b). At this point, there is flow reversal due to TEV formation which interacts with the leading edge feeding shear layer. This results in the separation of the LEV from the shear layer.

This mechanism of vortex detachment is similar to what is observed in flows past bluff-bodies (Widmann and Tropea 2015). Conversely, when $k \geq 0.12$, the relatively small oscillation time scales of the airfoil results in the maximum LEV circulation (Fig. 5a) and size (Fig. 5b) to be significantly reduced. That is, the LEV begins to form quite late in the downstroke, and thus the end of downstroke is reached before the LEV reaches its maximum possible circulation and size. The result is much lower peak values of the normalized strength of the LEV at higher reduced frequencies.

The normalized LEV circulation and diameter are plotted versus time using the shear layer-based convective time scale, c/\bar{U}_{SL} in Fig. 5c and d, respectively. For $k \leq 0.12$, the LEV circulation and diameter are shown to collapse to a single curve and their maximum respective values are attained at $t\bar{U}_{SL}/c \approx 4$, agreeing remarkably well with the concept of universal vortex formation time (Gharib et al. 1998). For $k \geq 0.12$, both the circulation and diameter also collapse well with the rest of the data in the early times during the cycle; however, as discussed above, their maximum values are much smaller than for $k \leq 0.10$. In addition, there seems to be no universal vortex formation time for these higher reduced

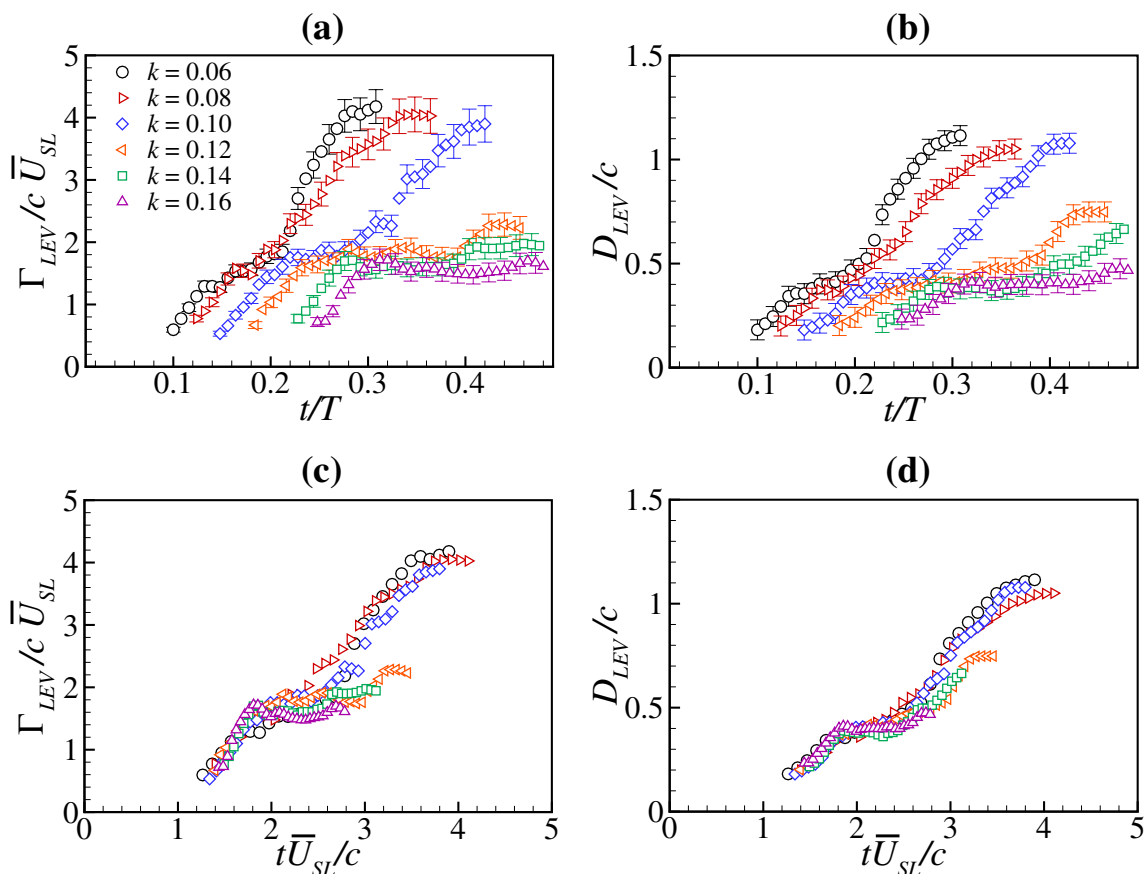


Fig. 5 **a** Normalized LEV circulation versus t/T , **b** normalized LEV diameter versus t/T , **c** normalized LEV circulation versus $t\bar{U}_{SL}/c$ and **d** normalized LEV diameter versus $t\bar{U}_{SL}/c$. For clarity, only every other data point is plotted

frequency values, but rather the maximum formation time is seen to decrease with increasing reduced frequency. Lastly, it may be interesting to note that for all reduced frequencies, the time of LEV inception occurs at $t\bar{U}_{SL}/c \approx 1.4$. This inception timescale was also observed by Siala et al. (2017) using the same reduced frequencies but different pitching and heaving amplitudes. This may suggest that the concept of optimal vortex formation may serve as a tool to predict the onset and growth of LEV circulation and size for combined heaving and pitching airfoils, at least for relatively low reduced frequencies which are greatly influenced by the LEV dynamics.

In Fig. 6a the chord-normal trajectory of the LEV, Y_{LEV}/c , is plotted versus t/T for all reduced frequencies. After LEV formation, the LEV remains very close to the airfoil surface ($Y_{LEV}/c = 0$) for a very short period of time. Meanwhile, the LEV is shown to convect along the chord at approximately the same rate for all reduced frequencies until it approaches the airfoil mid-chord ($X_{LEV}/c = 0$), as is shown in Fig. 6b. Afterwards, the LEV begins to travel away from the airfoil surface, while it remains approximately stationary near the mid-chord for $k \leq 0.10$. For $k \geq 0.12$, however, the LEV does not stop convecting in the stream-wise direction, but its rate of advection is slightly reduced.

Eventually the rate of LEV chord-wise advection increases again and it approaches a constant value while it is being shed into the wake ($X_{LEV}/c < -0.5$). This is accompanied by a reduction in the rate of chord-normal trajectory, as shown in Fig. 6a. In fact, for $k \geq 0.08$, the LEV is shown to move back towards the airfoil surface. Note that this reversed motion of the LEV only occurs once the LEV travels beyond the airfoil mid-chord, $X_{LEV}/c = 0$. Therefore as the airfoil begins to pitch back up in clock-wise direction at $t/T \approx 0.25$, the latter half of the airfoil moves downwards and hence it gets closer to the LEV. On the other hand for $k = 0.06$, the LEV slows down at $t/T \approx 0.23$ and then moves away quite rapidly again at $t/T \approx 0.26$. We believe this is associated with the fact that at $k = 0.06$, a very large TEV forms relatively early in the cycle, around which the LEV has to travel, thus pushing it away from the airfoil surface. It is possible that the LEV at this reduced frequency eventually moves back towards the airfoil surface after it completely travels around the TEV, but this cannot be confirmed as the field of view is not large enough to capture this process.

In Fig. 6c and d, the chord-normal and chord-wise LEV trajectories of the LEV are plotted versus $t\bar{U}_{SL}/c$. It is shown that the chord-normal LEV trajectories collapse quite well

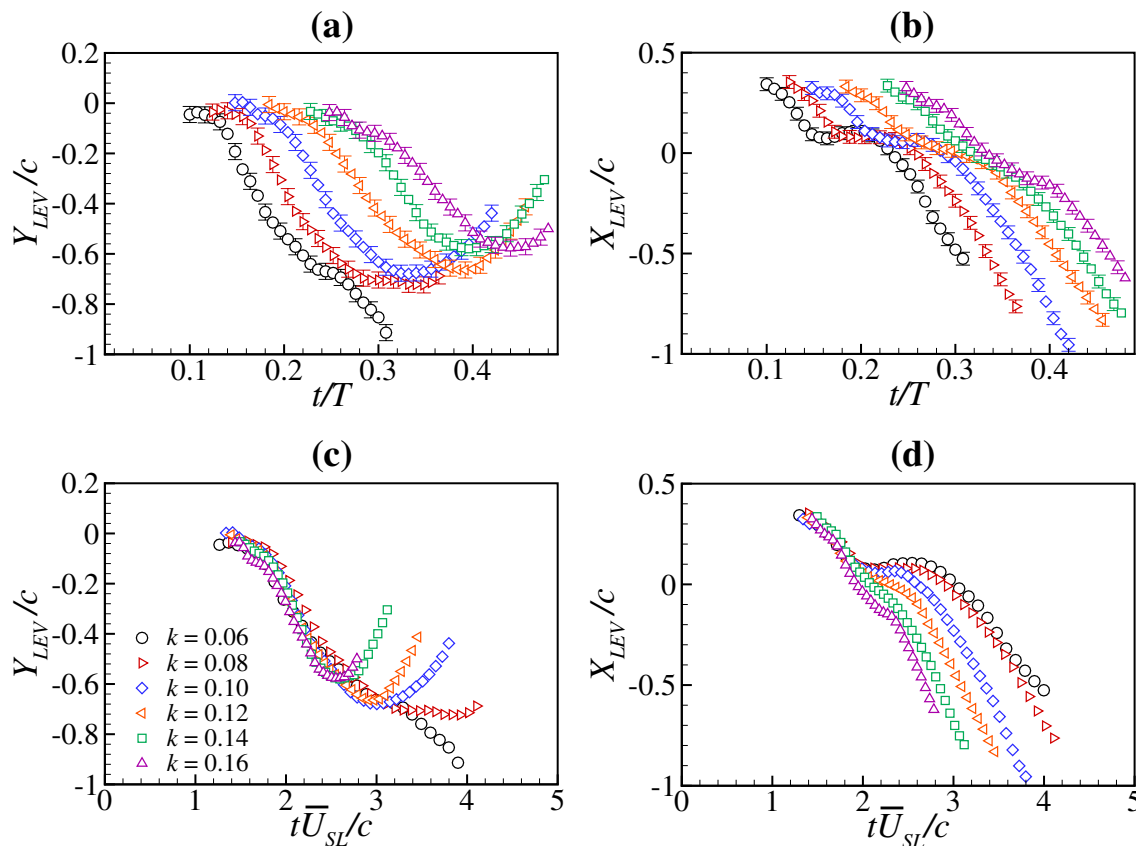


Fig. 6 **a** LEV normal trajectory versus t/T , **b** LEV axial trajectory versus t/T , **c** LEV normal trajectory versus $t\bar{U}_{SL}/c$ and **d** LEV axial trajectory versus $t\bar{U}_{SL}/c$. For clarity, only every other data point is plotted

from the inception time up until the reversed motion of LEV. Furthermore, the chord-wise trajectory is shown to collapse only up to $t\bar{U}_{sl}/c \approx 2$. Beyond this time, the trajectory becomes highly dependent on the value of the reduced frequency. The impact of LEV trajectory on the lift force production is discussed later in the paper.

3.1.1 Application of impulse equation to experimental data

Before presenting force results it is necessary to examine the effects of origin location when evaluating the terms. Although the impulse-based force equation is theoretically independent of the origin location (\mathbf{x}_0), the presence of errors in the data can be significantly amplified by the origin location. As mentioned by DeVoria et al. (2014) and Rival and Van Oudheusden (2017), the error amplification due to the selection of the origin location in the current approach is similar to that resulting from the selection of the reference pressure location in the direct integration of the Navier-Stokes equation. DeVoria et al. (2014) developed a technique that yields the origin location that mitigates the amplified error. This technique utilizes the DMT identity to relate the local and convective accelerations (which are used to remove the pressure term, see DeVoria et al. (2014) for a complete discussion) with other terms that contain only the measured velocity. The contribution of the viscous stress is not taken into account in this analysis because its influence on the forces is often negligible (as is shown later). The DMT (which is valid for any vector) is written here for the two vector quantities that are associated with the local and convective accelerations, respectively:

$$(N - 1) \int \mathbf{u}dV = \int (\mathbf{x} - \mathbf{x}_0) \times \boldsymbol{\omega}dV - \oint_{S+S_B} (\mathbf{x} - \mathbf{x}_0) \times \mathbf{n} \times \mathbf{u}dS \tag{9}$$

$$-(N - 1) \oint_S \frac{1}{2}(\mathbf{u} \cdot \mathbf{u})\mathbf{n}dS = \oint_S (\mathbf{x} - \mathbf{x}_0) \times \mathbf{n} \times [\mathbf{u} \cdot \nabla \mathbf{u} + \mathbf{u} \times \boldsymbol{\omega}]dS \tag{10}$$

where the subscript $S + S_B$ indicates that the surface integral is performed at the exterior surface S and the airfoil surface S_B . Note that for the local acceleration condition in Eq. (9), the velocity time derivative is not used to ensure that the error associated with the temporal discretization does not propagate in defining the origin location. The idea here is to determine the origin location \mathbf{x}_0 that best satisfies the left-hand side of both equations (which involve only the measured velocity). The objective origin is defined as the one that best satisfies the summation of these equations on a component-wise basis. This is determined as the origin which yields the smallest root mean square deviation (RMSD) over time between the left- and right-hand sides of the summation of Eqs. (9) and (10). The random velocity errors in the left-hand side leads to negligible error accumulation (DeVoria et al. 2014). In this study the flow is assumed to be two-dimensional and thus N is set to 2. Since we are interested in the lift force, the analysis is conducted for the y component only because the x moment arm plays a much bigger role in the lift production than the y moment arm (Noca 1997). Equations (9) and (10) are non-dimensionalized by $\frac{1}{2}U_\infty^2 Tc$ and $\frac{1}{2}U_\infty^2 c$, respectively. We calculate the RMSD for 3600 origins uniformly distributed over the entire measurement plane. Figure 7a shows a contour plot of the RMSD (in percentage of the maximum value of the sum) as a function of the origin location for $k = 0.06$. Figure 7b displays the coordinate system that is used. As shown, the RMSD is strongly dependent on the origin of the x -axis, while its dependence on the y axis is essentially insignificant. It is shown in Fig. 7a that the RMSD is minimized at

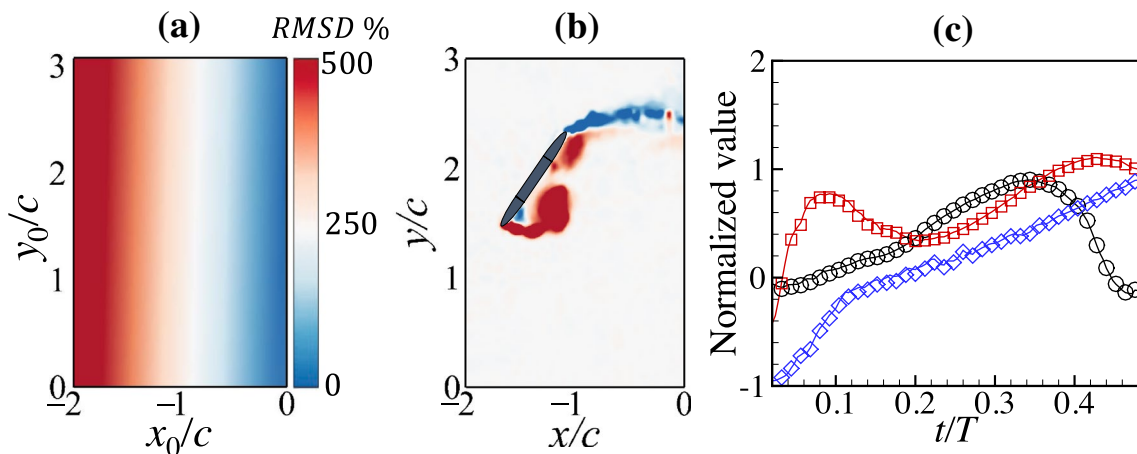


Fig. 7 a Contour of the root mean square deviation between the left- and right-hand side of the sum of Eqs. (9) and (10), b coordinate system and c comparison of the sum of the left-hand side (solid lines)

with the sum of the right- hand side (symbols) of Eqs. (9) and (10) using the objectively defined origin. The black, red and blue colors represent $k = 0.06, 0.10$ and 0.14 , respectively

the downstream boundary ($x_0/c = 0$) of the control volume (at this location the RMSD varies from 1.2% of the maximum value to 3.5%, depending on y_0). The contour distribution of the RMSD is found to be essentially identical for all reduced frequencies tested. Figure 7c compares the sum of the left-hand side (solid lines) with the sum of the right-hand side (symbols) of Eqs. (9) and (10) for $x_0/c = 0$, showing excellent agreement.

In addition, an analysis was conducted to investigate the effects of control volume size on the origin location as well as the calculated transient lift force. Six control volumes were tested, which are shown in Fig. 8a. We varied the control volume size by adjusting the distance from the airfoil trailing edge to the downstream boundary (s/c). The largest control volume corresponds to a distance of 1 chord length from the trailing edge to the downstream boundary, whereas the smallest control volume corresponds to a distance of $0.25c$. The cross-stream size of the control volume was found to have a negligible influence on the results. For all control volumes tested, the objective origin was always located at the downstream boundary with RMSD values below 4 %. Figure 8b shows the effect of control volume size on the calculated lift coefficient ($C_y = 2F_y/\rho U_\infty^2 c$) for $k = 0.06$. It is shown that the transient lift force is significantly altered by the distance of the downstream boundary to the airfoil trailing edge when $s/c < 0.85$. As s/c is decreased, the time at which the force begins to deviate from the converged force estimate (i.e. when $s/c > 0.85$) is shifted to earlier times. For example when $s/c = 0.25$, the force begins to deviate from the converged force estimate at $t/T \approx 0.19$, whereas for $s/c = 0.55$, the deviation occurs $t/T \approx 0.23$. For all reduced frequencies considered in this study, the force deviation from the converged estimate seems to occur only when the LEV advects outside of the control volume while it is still growing (i.e. entraining vorticity from the shear layer). When s/c increases, there is sufficient area for the

LEV to reach its maximum circulation before it begins to advect outside of the control volume. This effect is quite interesting and will be thoroughly addressed in a future publication. For the remainder of this paper, we use the largest control volume ($s/c = 1$) to conduct the rest of our analysis.

3.1.2 Reduction of the impulse equation

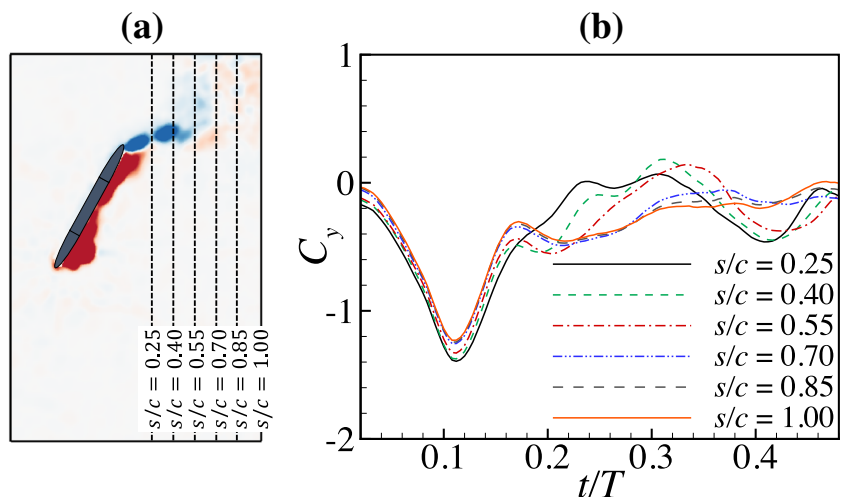
For convenience, the impulse-based force equation for a two dimensional flow is rewritten:

$$\begin{aligned}
 \mathbf{F} = & \underbrace{-\frac{\rho}{N-1} \frac{d}{dt} \int_{V_f} (\mathbf{x} - \mathbf{x}_0) \times \boldsymbol{\omega} dV}_{T1} + \underbrace{\rho \oint_S \mathbf{n} \cdot \left(\frac{1}{2} u^2 \mathbf{I} - \mathbf{u} \otimes \mathbf{u} \right) dS}_{T2} \\
 & + \underbrace{\oint_S \mathbf{n} \cdot \boldsymbol{\lambda}_{\text{imp}} dS}_{T3} + \underbrace{\frac{\rho}{N-1} \frac{d}{dt} \oint_{S_b} (\mathbf{x} - \mathbf{x}_0) \times (\mathbf{n} \times \mathbf{u}) dS}_{T4}
 \end{aligned} \tag{11}$$

As was mentioned previously, the impulse force equation contains complex boundary integral terms that account for the finite control volume. The physical interpretation of these terms is not obvious, and therefore it is difficult to isolate the mechanisms responsible for the lift production. We now show that it is possible to greatly simplify this formulation through the use of the objectively determined origin defined in the previous section.

To calculate the transient lift force, the flow impulse (denoted as $T1$ in Eq. (11)) was fitted to a cubic spline prior to taking the time derivative. The time derivative was calculated using a central difference scheme with $dt = 0.004$ s. The results are filtered using an eight-point moving average to remove the high frequency fluctuations related to measurement noise from the force signal. Note that data in the first and last $t/T = 0.02$ of the downstroke are omitted due

Fig. 8 **a** A schematic of different control volumes used to test control volume and origin location dependence and **b** time-history of the lift force for various control volumes at $k = 0.06$



to unreliable fits. Figure 9 shows the total lift coefficient (C_y), as well as the contribution of each individual term of the impulse equation for $k = 0.06$ and 0.14 . As shown, the total lift coefficient is dominated by the first two terms, with the first, $T1$, dominant during the first part of the downstroke, and then a combination of $T1$ and $T2$ dominant during the remainder of the downstroke. The third and fourth terms, $T3$ and $T4$, are negligible during the entire cycle. The inertial force of the fluidic body ($T4$) is typically negligible for thin airfoils moving in air. The impulse flux force, $T3$, is evaluated on the control volume boundaries, and vortical structures leave the control volume mainly through the downstream boundary. It is apparent that this term is dependent on the streamwise origin location x_0 . By choosing an origin located at the downstream boundary, this term becomes negligible (though not exactly zero, because some vortices may leave the upper and lower boundaries of the control volume). These results are consistent with the suggestion by Noca (1997) that the impulse flux force contribution leads to the dilemmic dependence of the impulse force equation on the origin location. By locating the origin at the downstream boundary the contribution of $\mathbf{n} \cdot \mathbf{u}(\mathbf{x} \times \boldsymbol{\omega})$ is significantly reduced. This justification seems to resonate well with the objective origin definition proposed by DeVoria et al. (2014).

Based on the above arguments, the force equation can be simplified by retaining $T1$ and $T2$ as follows:

$$\mathbf{F} \approx -\rho \frac{d}{dt} \int (\mathbf{x} - \mathbf{x}_0) \times \boldsymbol{\omega} dA + \rho \oint_S \mathbf{n} \cdot \left(\frac{1}{2} u^2 \mathbf{I} - \mathbf{u} \otimes \mathbf{u} \right) dS \tag{12}$$

The first term is the rate of change of impulse, which represents the force produced by vortical structures within the control volume. This term consists of the contributions of the vortex circulation growth and advection to the transient lift force (Stevens and Babinsky 2017). Moreover, Saffman (1992) showed that for an impermeable body, the second

term on the right-hand side can be written in terms of the Lamb vector such as:

$$\oint_S \mathbf{n} \cdot \left(\frac{1}{2} u^2 \mathbf{I} - \mathbf{u} \otimes \mathbf{u} \right) dS = \int \mathbf{u} \times \boldsymbol{\omega} dA \tag{13}$$

Note that Saffman (1992) shows that the velocity within a vortex can be written as $\mathbf{u} = \mathbf{u}_v + \mathbf{u}_e$, where \mathbf{u}_v is the velocity induced by the vortex itself (which can be calculated using Bio-Savart law) and \mathbf{u}_e is the external velocity (Kang et al. 2018). The Lamb vector of the self-induced velocity of the vortex, $\int \mathbf{u}_v \times \boldsymbol{\omega} dV$, can be shown to equal zero, meaning that the total vortex force exerted by the vortex on itself is zero. Therefore the only contribution from the Lamb vector is $\int \mathbf{u}_e \times \boldsymbol{\omega} dA$. This can be interpreted as follows. The external velocity, which also includes the induced velocity by other vortical structures either inside or outside of the control volume, interacts with the vorticity of a specific vortex structure (e.g. LEV) within the control volume to produce a force on the airfoil. When the entire vorticity field is contained within the control volume, for example in starting flows, then the vortex force can be shown to equal zero. This suggests that the vortex force term due to vortices outside of the control volume can be thought of as a history effect of the vortex shedding in the far-wake.

Now that the impulse equation has been reduced to terms with clear physical meanings, the mechanisms responsible for the transient lift production can be analyzed. It can be noted that Eq. (12) is identical to the formulation developed by Kang et al. (2018) using the minimum-domain theory.

3.1.3 Transient lift force analysis

The transient lift coefficient is plotted in Fig. 10 for low and high reduced frequency ranges, $k = 0.06-0.10$ (Fig. 10a) and $k = 0.12-0.16$ (Fig. 10b). For the low reduced frequency range, the lift coefficient is shown to contain two peaks. The magnitude of the secondary peak, which occurs later in the

Fig. 9 Evaluation of the four terms of Eq. (11) contributing to the lift force in the impulse equation as well as the total lift force for **a** $k = 0.06$ and **b** $k = 0.14$. For clarity, only every other data point is plotted

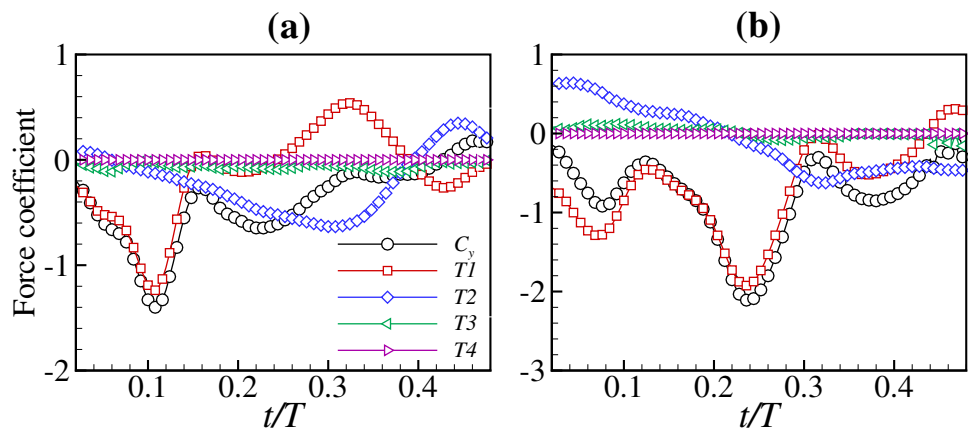
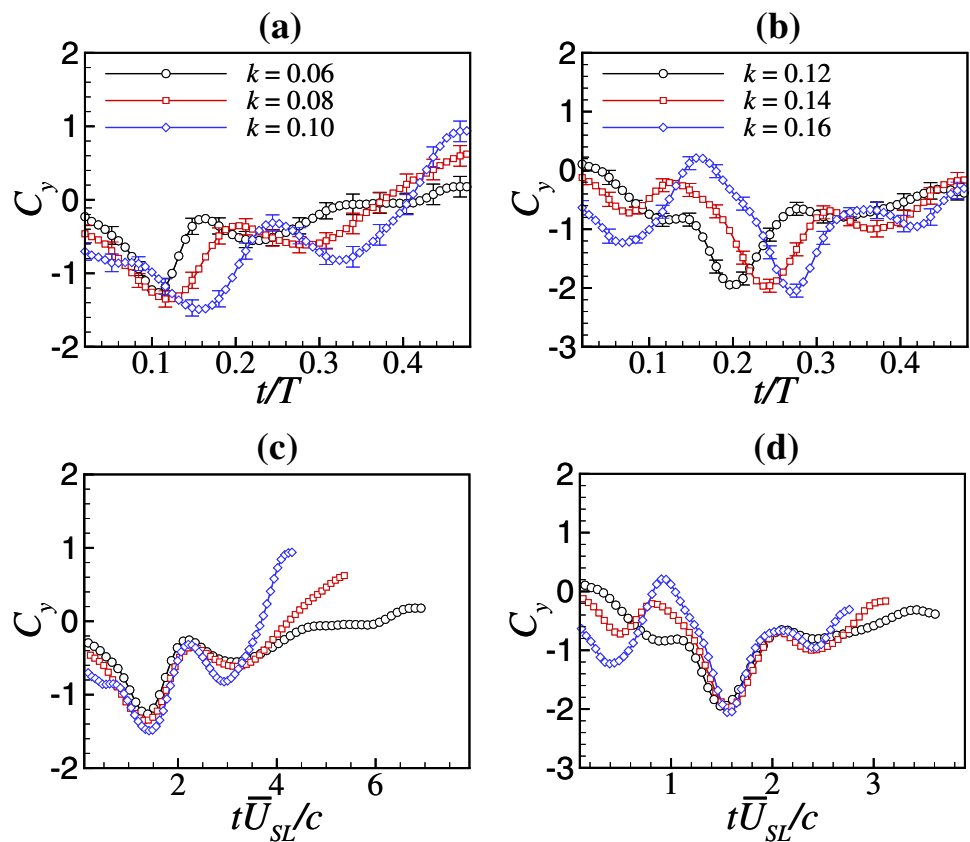


Fig. 10 Transient lift coefficient versus t/T for **a** $k = 0.06–0.10$ and **b** $k = 0.12–0.16$. Transient lift coefficient versus $t\bar{U}_{SL}/c$ for **c** $k = 0.06–0.10$ and **d** $k = 0.12–0.16$



downstroke, is approximately 50–55% of the magnitude of the primary peak. The timing of both the primary and secondary peaks is delayed, and their magnitudes increase with increasing reduced frequency. For all reduced frequencies, the lift coefficient approaches positive values (i.e. opposite direction of lift) by the end of the cycle, where the magnitude also increases with increasing reduced frequency. The generation of two lift peaks for heaving and pitching airfoils has been reported in the literature by several researchers (Deng et al. 2014; Karbasian et al. 2016; Totpal et al. 2017). Furthermore, the high reduced frequency cases also show that an additional tertiary lift peak is produced early in the downstroke, whose magnitude relative to the primary peak lift increases with increasing reduced frequency. Similar to the smaller reduced frequency range, the primary and secondary peaks increase in magnitude and are delayed in time as k increases. It is seen that the lift coefficients at high reduced frequencies do not approach positive values at the end of the cycle.

Figure 10c and d shows results using a rescaling of the cycle time that is based on the leading-edge velocity as $t\bar{U}_{SL}/c$. Interestingly, the primary peak force that occurs near $t\bar{U}_{SL}/c \approx 1.75$, is consistent for all reduced frequencies. Also, the value of this convective time scale is slightly after the time at which the LEV is initiated (see Fig. 5c). This seems to imply that the roll-up of the leading-edge shear

layer into an LEV is the dominant mechanism of peak lift production. It also indicates that the leading-edge velocity scaling of the time of this peak is explicitly independent of the reduced frequency since this scaling collapses the data over this reduced frequency range. For the lower range of reduced frequencies in Fig. 10c the lift coefficient is shown to collapse fairly well up until the local minimum just after the primary peak is produced. For time $t\bar{U}_{SL}/c > 3.7$ the lift coefficients begin to diverge. This corresponds to the time at which the trailing-edge shear layer begins to roll-up into a TEV. The results for the larger range of reduced frequencies in Fig. 10d show somewhat different trends. For these cases the TEV does not form and hence the lift coefficients do not significantly diverge at later times during the cycle. Also, for the larger reduced frequencies, the influence of the lagging LEV from the previous cycle near the top heaving position results in a third minor peak at early times in the cycle. The strength of this minor peak increases with increases reduced frequency while occurring earlier at the start of the downstroke. In fact, it is only this early cycle minor peak that distinguishes the effect of increasing reduced frequencies for the high k values.

To better understand the role of vortical structures, in particular the LEV and TEV, in lift force production, it is necessary to correlate them with the transient lift force. Rather than using the vorticity field alone, we use the local

integrand of the impulse and vortex forces of Eq. (12). For the vortex force, the lamb vector is used instead of the flux formulation to visualize its local contribution within the control volume. Figure 11 shows the total lift coefficient (C_y) for $k = 0.06$, as well as the contributions of the impulse ($C_{y,I}$) and vortex ($C_{y,V}$) forces. In addition, contours of vorticity and the integrand of impulse ($F_{y,I}$) and vortex ($F_{y,V}$) forces for five snapshots during the downstroke motion are provided. Both force integrands are normalized by $2c/\rho U_\infty^2$. In snapshot (1), the LEV had just been formed, and it remains compact and quite close to the airfoil surface. The impulse force contour plot shows that the LEV is primarily producing a negative impulse (in the direction of lift). The total lift here is dominated by the LEV impulse force. While the LEV is shown to produce a vortex force, its contribution is approximately cancelled by the vortex force produced by the trailing-edge shear layer, hence $C_{y,V} \approx 0$. Slightly after peak force production in snapshot (1), the LEV begins to lift-off from the airfoil surface. As a result, the total lift is reduced from $C_y \approx -1.2$ to $C_y \approx -0.5$ in snapshot (2). This reduction in force is a consequence of the low pressure zone generated by the LEV being relatively far away from the airfoil, which reduces the pressure difference between the upper and lower surfaces. From the impulse analysis point of view, the LEV begins to produce a positive impulse force (lift-diminishing) that approximately cancels the negative impulse contribution (lift-enhancing), such that $C_{y,I} \approx 0$. Additionally, the LEV is also shown to produce a positive vortex force (lift-diminishing), however, the lift-enhancing

effect clearly dominates. The total lift force at this snapshot is primarily due to the vortex force of the LEV.

The fact that the LEV produces lift-enhancing as well as lift-diminishing impulse and vortex forces is quite interesting. Contrary to the conventional belief that LEVs on the suction side only provide lift-enhancing contributions, it is necessary to stress that there is no vortical structure that provides a purely single-sign contribution to the aerodynamic forces. Wu et al. (2007) have observed a similar phenomena for drag force analysis for a flow past a cylinder. They explained that this observation is consistent with the fact that attached flows over an airfoil produce boundary layers at the upper and lower surfaces of the airfoil, but only the sum of the total vorticity in the boundary layer (i.e. net circulation) yields the desired lift. Furthermore, an alternative explanation of the significant lift reduction in snapshot (2) can be understood by decomposing the force impulse into circulation growth and chord-wise trajectory of the LEV (refer to Section 4.3.2). At this instant in time ($t/T \approx 0.16$), the rate of change of LEV circulation significantly decreases (Fig. 5a) and the LEV chord-wise advection approaches zero (Fig. 6b). Consequently, the LEV impulse force contribution is greatly decreased. The magnitude of the secondary lift peak in (3) is also shown to be dominated almost entirely by the vortex force produced by the LEV and its shear layer. The formation of the peak itself, however, is a result of the impulse force becoming less negative and ultimately going positive near $t/T \approx 0.25$. This is equivalent to the convective time scale of $tU_{SL}/c \approx 3.7$, at which the TEV begins to form. In snapshot (4), the total lift force is shown to drop to

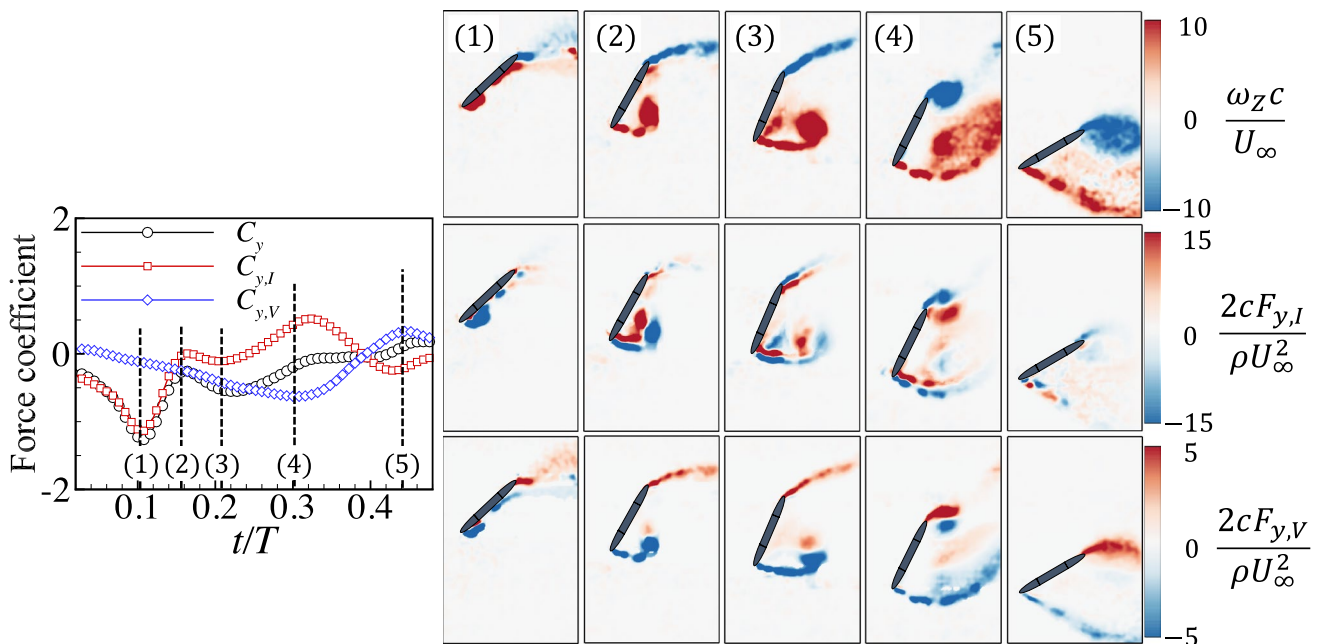


Fig. 11 Synchronization of the transient lift force with the vorticity field and the local contours of the impulse and vortex forces for $k = 0.06$

very small values. The LEV here has attained its maximum circulation (see Fig. 5a at $t/T \approx 0.30$), and thus no longer contributes to the force impulse. In addition, its advection relative to the TEV is also expected to significantly drop as it approaches the trailing edge of the airfoil (Stevens and Babinsky 2017). Meanwhile, the rolled-up TEV begins to generate a net positive impulse force (i.e. lift-diminishing), which almost cancels with the vortex force produced by the leading-edge shear layer and TEV. Beyond snapshot (4), the LEV begins to convect outside of the control volume, which is reflected by the impulse force going from positive to negative values in snapshot (5). This is accompanied by the change of the sign of the vortex force from positive to negative. IN snapshot (5) and beyond, the TEV begins to leave the control volume, and the impulse force decays from negative values to zero, whereas the Lamb force decays from positive values to zero, hence they cancel each other to result in $C_y \approx 0$ by the end of the downstroke. This equal and opposite trend of the Lamb and impulse forces indicates that the Lamb vector is indeed picking up the contribution of the LEV and TEV as they leave the control volume.

As the reduced frequency is increased to $k = 0.14$, the third lift peak is formed early in the cycle, as shown in snapshot (1) for $k = 0.14$ in Fig. 12. The negative LEV generated from the previous upstroke is shown to be captured by the airfoil as it begins heaving/pitching downward. The majority of the impulse force is shown to be sporadically distributed within the separated flow on the upper surface of the airfoil. It should be kept in mind that $F_{y,I}$ is calculated locally and therefore the noise level due to spatial and temporal

derivatives may be high. However, the integrated value ($C_{y,I}$) clearly dominates the total lift production. Furthermore, the small positive vortex force at this instant is shown to be dominated by the upper-surface shear layer. In snapshot (2), this lift-enhancing effect has subsided and the upper shear layer begins to re-attach to the airfoil surface. The lift here is dominated by the impulse force from the nearly-attached boundary layer. However, we anticipate that the accuracy of the force calculation here to be somewhat hindered by the fact that the PIV measurements do not fully resolve the surface vorticity. The mechanism responsible for the production of peak force in snapshot (3) is identical to the mechanism identified for the lower reduced frequency value. In snapshot (4), it is shown that the secondary peak force is a result of the slight increase (in the negative direction) of the impulse force $C_{y,I}$. Since the LEV is no longer growing at this instant of time (see Fig. 5a), the increase of the impulse force can then be associated with the enhanced chord-wise advection of the LEV (i.e. the slope of the chord-wise LEV position increases at this instant, as shown in Fig. 6b). Furthermore, a notable difference at this large reduced frequency case is the lack of TEV formation. As explained in the previous section, the LEV approaches the trailing edge of the airfoil quite late in the downstroke, where the angle of attack is not large enough to support the roll-up of the trailing-edge shear layer into a TEV. Consequently, the lift-diminishing effect of the TEV is avoided.

To conclude the above discussion, the lift-enhancing mechanisms for the low reduced frequency range ($k = 0.06 - 0.10$) are all related to the LEV generation, its growth and its

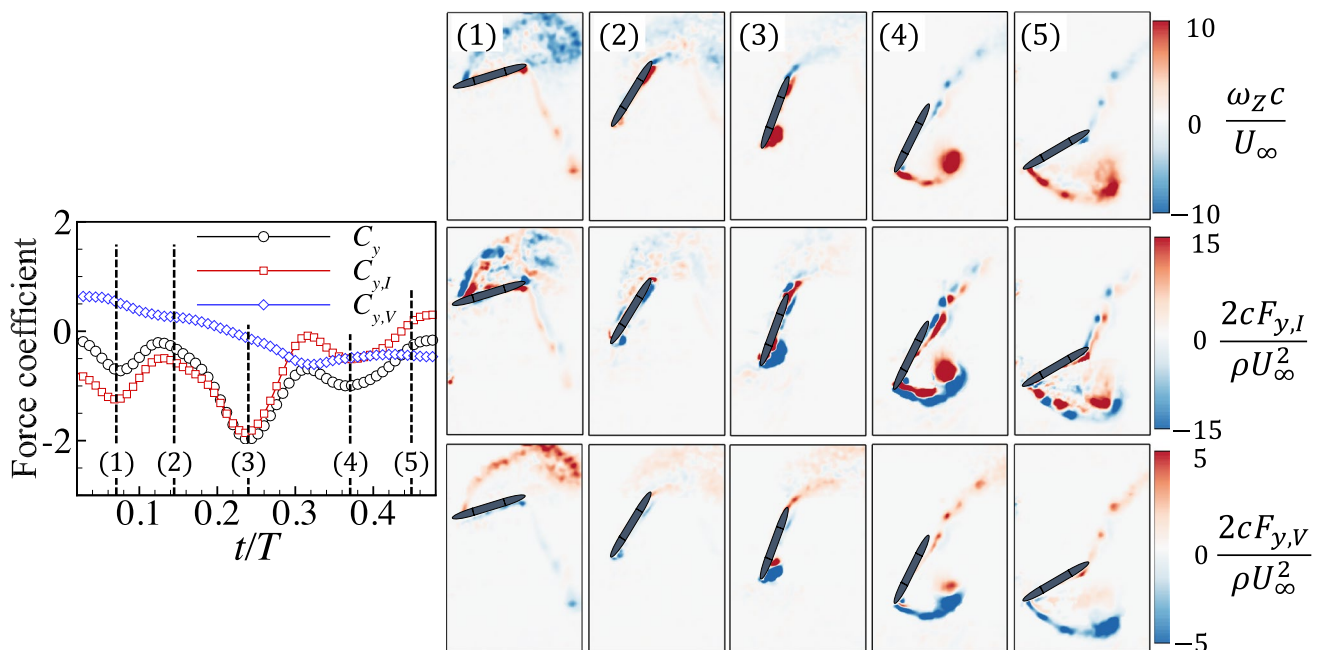


Fig. 12 Synchronization of the transient lift force with the vorticity field and the local contours of the impulse and vortex forces for $k = 0.14$

trajectory relative to the airfoil surface. As the reduced frequency is increased to $k = 0.12 - 0.16$, the slower convective time scale of the vortical structures allows the airfoil to capture the influence of the previously shed LEV, whereas the lift-diminishing effect of the TEV is avoided. It is interesting to note the optimal vortex formation generated for the low-frequency cases does not correlate with the peak lift. This contradicts the findings of Milano and Gharib (2005), who show that the peak lift force is produced when the LEV formation number reaches approximately 4. However, their results are for a flapping wing (pitching) while translating (not heaving) which does not have the same effect on the trajectory of the leading-edge vortex motion relative to the surface. We believe that this discrepancy of lift force versus formation number is related to the fact that the LEV generated in our experiments begins to lift-off from the airfoil surface much before the optimal formation number is achieved. Therefore the correlation between the optimal vortex formation number and maximum lift production is not only dependent on the LEV size and strength, but also on the LEV trajectory relative to the airfoil. At larger values of k our results show that an optimal formation number is never reached due to the disconnection of the feeding shear layer from the leading-edge vortex. For energy harvesting applications where it is important to correlate peak force with peak heaving velocity during the cycle, the delayed leading-edge vortex formation associated with higher k values improves power production even though the peak formation numbers are lower. Lastly, for all reduced frequencies, the impulse force produces the general trend of the transient lift, whereas the vortex force simply modifies the lift magnitude. The implication of this is that unlike impulsively moving airfoils where the entire circulatory force is dominated by the impulse force (Stevens and Babinsky 2017), the contribution of the vortex force must be taken into consideration when constructing low-order lift models of continuously oscillating airfoils.

4 Conclusions

In this paper, two-dimensional particle image velocimetry measurements were conducted to investigate the vortex dynamics and lift force production mechanisms of an oscillating airfoil undergoing dynamic stall at reduced frequencies of $k = 0.06 - 0.16$. The transient lift force was estimated from the velocity fields and its derivatives using the derivative moment transformation-based impulse force formulation. The moment-arm dilemma associated with the application of the force impulse equation to experimental data was investigated. It is shown that the origin location that most effectively reduces the amplified error due to the position vector was always located at the downstream boundary of the control volume. In addition, it was found that the calculated lift forces

were consistent when the distance from the airfoil trailing edge to the downstream boundary was equal to and greater than $0.85c$. Upon using the objectively defined origin, the impulse force equation was shown to reduce to two dominating terms: the rate of change of the impulse within the control volume and the Lamb vector thereof that picks up the contribution of vortices outside of the control volume.

For $k = 0.06 - 0.10$, the lift force results show that there are two force peaks that form during the downstroke/upstroke. The primary peak is associated with the formation of the leading-edge vortex and the secondary peak is associated with its enhanced time rate of circulation growth and chord-wise advection. Even though the optimal leading-edge vortex formation number was attained for these lower reduced frequencies, it was observed that its timing was not well correlated with the timing of maximum lift force. In addition, at this low reduced frequency range, the trailing vortex sheet was observed to roll-up into a trailing-edge vortex. The trailing-edge vortex was shown to produce lift-diminishing effects, whose intensity increases with increasing reduced frequency. For $k = 0.12 - 0.16$, a third lift peak was shown to form at the beginning of the downstroke due to a vortex capture-like effect from the LEV shed during the previous upstroke. No trailing-edge vortex formation was observed at these high reduced frequencies, hence the lift-diminishing effect was avoided.

The results of this study may be of great importance in developing low-order models of transient lift forces produced by oscillating airfoils undergoing dynamic stall. In particular, the overall trend of the lift force was shown to be primarily dependent on the impulse force produced by vortical structures (leading and trailing-edge vortices and their associated shear layers) within the control volume. However, the Lamb force, which indirectly captures the influence of the far-field vortical structures may significantly alter the magnitude of lift. The implication of this is that the influence of vortical structures in the far-field must also be considered when constructing low-order models.

Acknowledgements The authors would like to thank Dr. Ali Mousavian and Cameron Planck for helping with designing the heaving/pitching device and developing the LabView code. Firas Siala acknowledges the financial support from Link Energy Foundation Fellowship. Financial support was provided through the National Science Foundation, Award number 1804964. Also, financial support was provided through the Air Force Office of Scientific Research under the MURI Grant FA9550-07-1-0540.

References

- Babinsky H, Stevens RJ, Jones AR, Bernal LP, OI MV (2016) Low order modelling of lift forces for unsteady pitching and surging wings. In: 54th AIAA Aerospace Sciences Meeting, pp 290

- Baik Y S, Bernal L, Shyy W, Ol M (2011) Unsteady force generation and vortex dynamics of pitching and plunging flat plates at low Reynolds number. In: 49th AIAA Aerospace Sciences Meeting including the New Horizons Forum and Aerospace Exposition, pp 220
- Baik YS, Bernal LP, Granlund K, Ol MV (2012) Unsteady force generation and vortex dynamics of pitching and plunging aerofoils. *J Fluid Mech* 709:37–68
- Batchelor GK (2000) An introduction to fluid dynamics. Cambridge University Press, Cambridge
- Brown C (1954) Effect of leading-edge separation on the lift of a delta wing. *J Aeronaut Sci* 21(10):690–694
- Charonko JJ, King CV, Smith BL, Vlachos PP (2010) Assessment of pressure field calculations from particle image velocimetry measurements. *Meas Sci Technol* 21(10):105401
- Dabiri JO (2009) Optimal vortex formation as a unifying principle in biological propulsion. *Annu Rev Fluid Mech* 41:17–33
- Dabiri JO, Bose S, Gemmell BJ, Colin SP, Costello JH (2014) An algorithm to estimate unsteady and quasi-steady pressure fields from velocity field measurements. *J Exp Biol* 2014:jeb-092767
- Darakananda D, Eldredge J, Colonius T, Williams DR (2016) A vortex sheet/point vortex dynamical model for unsteady separated flows. In: 54th AIAA aerospace sciences meeting, pp 2072
- Deng J, Caulfield C, Shao X (2014) Effect of aspect ratio on the energy extraction efficiency of three-dimensional flapping foils. *Phys Fluids* 26(4):043102
- DeVoria AC, Carr ZR, Ringuette MJ (2014) On calculating forces from the flow field with application to experimental volume data. *J Fluid Mech* 749:297–319
- Dunne R, McKeon BJ (2015) Dynamic stall on a pitching and surging airfoil. *Exp Fluids* 56(8):157
- Eldredge JD, Jones AR (2019) Leading-edge vortices: mechanics and modeling. *Annu Rev Fluid Mech* 51:75–104
- Ellington CP (1999) The novel aerodynamics of insect flight: applications to micro-air vehicles. *J Exp Biol* 202(23):3439–3448
- Ellington CP, Van Den Berg C, Willmott AP, Thomas AL (1996) Leading-edge vortices in insect flight. *Nature* 384(6610):626
- Epps BP (2010) An impulse framework for hydrodynamic force analysis: fish propulsion, water entry of spheres, and marine propellers. In: PhD thesis, Massachusetts Institute of Technology
- Ford CP, Babinsky H (2013) Lift and the leading-edge vortex. *J Fluid Mech* 720:280–313
- Gharib M, Rambod E, Shariff K (1998) A universal time scale for vortex ring formation. *J Fluid Mech* 360:121–140
- Graftieaux L, Michard M, Grosjean N (2001) Combining pIV, PIV and vortex identification algorithms for the study of unsteady turbulent swirling flows. *Meas Sci Technol* 12(9):1422
- Hammer P, Altman A, Eastep F (2014) Validation of a discrete vortex method for low Reynolds number unsteady flows. *AIAA J* 52(3):643–649
- Hubel TY, Tropea C (2010) The importance of leading edge vortices under simplified flapping flight conditions at the size scale of birds. *J Exp Biol* 213(11):1930–1939
- Hubel TY, Hristov NI, Swartz SM, Breuer KS (2009) Time-resolved wake structure and kinematics of bat flight. *Exp Fluids* 46(5):933
- Kang L, Liu L, Su W, Wu J (2018) Minimum-domain impulse theory for unsteady aerodynamic force. *Phys Fluids* 30(1):016107
- Karbasian H, Esfahani JA, Barati E (2016) The power extraction by flapping foil hydrokinetic turbine in swing arm mode. *Renew Energy* 88:130–142
- Kármán TV (1938) Airfoil theory for non-uniform motion. *J Aeronaut Sci* 5(10):379–390
- Kim D, Hussain F, Gharib M (2013) Vortex dynamics of clapping plates. *J Fluid Mech* 714:5–23
- Lamb H (1932) Hydrodynamics. Cambridge University Press, Cambridge
- Leishman JG (1994) Unsteady lift of a flapped airfoil by indicial concepts. *J Aircraft* 31(2):288–297
- Li G-J, Lu X-Y (2012) Force and power of flapping plates in a fluid. *J Fluid Mech* 712:598–613
- Lighthill J (1986) Fundamentals concerning wave loading on offshore structures. *J Fluid Mech* 173:667–681
- Lin J-C, Rockwell D (1996) Force identification by vorticity fields: techniques based on flow imaging. *J Fluids Struct* 10(6):663–668
- Liu X, Katz J (2006) Instantaneous pressure and material acceleration measurements using a four-exposure PIV system. *Exp Fluids* 41(2):227
- Liu Z, Lai JC, Young J, Tian F-B (2016) Discrete vortex method with flow separation corrections for flapping-foil power generators. *AIAA J* 55(2):410–418
- Lua K, Zhang X, Lim T, Yeo K (2015) Effects of pitching phase angle and amplitude on a two-dimensional flapping wing in hovering mode. *Exp Fluids* 56(2):35
- Mackowski A, Williamson C (2015) Direct measurement of thrust and efficiency of an airfoil undergoing pure pitching. *J Fluid Mech* 765:524–543
- Madangopal R, Khan ZA, Agrawal SK (2005) Biologically inspired design of small flapping wing air vehicles using four-bar mechanisms and quasi-steady aerodynamics. *J Mech Des* 127(4):809–816
- Milano M, Gharib M (2005) Uncovering the physics of flapping flat plates with artificial evolution. *J Fluid Mech* 534:403–409
- Mohebbian A, Rival DE (2012) Assessment of the derivative-moment transformation method for unsteady-load estimation. *Exp Fluids* 53(2):319–330
- Moriche M, Flores O, Garcia-Villalba M (2017) On the aerodynamic forces on heaving and pitching airfoils at low Reynolds number. *J Fluid Mech* 828:395–423
- Morse DR, Liburdy JA (2009) Vortex dynamics and shedding of a low aspect ratio, flat wing at low Reynolds numbers and high angles of attack. *J Fluids Eng* 131(5):051202
- Noca F (1997) On the evaluation of time-dependent fluid-dynamic forces on bluff bodies. PhD dissertation, Pasadena
- Onoue K, Breuer KS (2016) Vortex formation and shedding from a cyber-physical pitching plate. *J Fluid Mech* 793:229–247
- Platzer MF, Jones KD, Young J, Lai SJ (2008) Flapping wing aerodynamics: progress and challenges. *AIAA J* 46(9):2136–2149
- Ramesh K, Gopalarathnam A, Granlund K, Ol MV, Edwards JR (2014) Discrete-vortex method with novel shedding criterion for unsteady aerofoil flows with intermittent leading-edge vortex shedding. *J Fluid Mech* 751:500–538
- Rival DE, Van Oudheusden B (2017) Load-estimation techniques for unsteady incompressible flows. *Exp Fluids* 58(3):20
- Rival D, Prangemeier T, Tropea C (2009) The influence of airfoil kinematics on the formation of leading-edge vortices in bio-inspired flight. *Exp Fluids* 46(5):823–833
- Rival DE, Kriegseis J, Schaub P, Widmann A, Tropea C (2014) Characteristic length scales for vortex detachment on plunging profiles with varying leading-edge geometry. *Exp Fluids* 55(1):1660
- Saffman PG (1992) Vortex dynamics. Cambridge University Press, Cambridge
- Sciacchitano A, Wieneke B (2016) PIV uncertainty propagation. *Meas Sci Technol* 27(8):084006
- Siala FF, Prier MW, Liburdy JA (2018) Force production mechanisms of a heaving and pitching foil operating in the energy harvesting regime. In: ASME 2018 5th Joint US-European Fluids Engineering Division Summer Meeting, pp V001T07A002–V001T07A002. American Society of Mechanical Engineers
- Siala FF, Totpal AD, Liburdy JA (2017) Optimal leading edge vortex formation of a flapping foil in energy harvesting regime. In: ASME 2017 Fluids Engineering Division Summer Meeting, pp

- V01CT23A008–V01CT23A008. American Society of Mechanical Engineers
- Siala F, Liburdy JA (2015) Energy harvesting of a heaving and forward pitching wing with a passively actuated trailing edge. *J Fluids Struct* 57:1–14
- Srygley R, Thomas A (2002) Unconventional lift-generating mechanisms in free-flying butterflies. *Nature* 420(6916):660
- Stevens P, Babinsky H (2017) Experiments to investigate lift production mechanisms on pitching flat plates. *Exp Fluids* 58(1):7
- Tchieu AA, Leonard A (2011) A discrete-vortex model for the arbitrary motion of a thin airfoil with fluidic control. *J Fluids Struct* 27(5–6):680–693
- Theodorsen T (1934) Naca report 496: general theory of aerodynamic instability and the mechanism of flutter. In: Advisory Committee for Aeronautics, Technical report, VA, USA
- Torbert S (2016) Applied computer science. Springer, Berlin
- Totpal AD (2017) The energy extraction performance of an oscillating rigid and flexible foil. Ms thesis, Oregon State University, Corvallis
- Totpal AD, Siala FF, Liburdy JA (2017) Flow energy harvesting of an oscillating foil with rigid and passive surface flexibility. In: ASME 2017 Fluids Engineering Division Summer Meeting, pp V01CT19A002–V01CT19A002. American Society of Mechanical Engineers
- Tuncer IH, Platzer MF (2000) Computational study of flapping airfoil aerodynamics. *J Aircr* 37(3):514–520
- Van Oudheusden B (2013) Piv-based pressure measurement. *Meas Sci Technol* 24(3):032001
- Villegas A, Diez FJ (2014) On the quasi-instantaneous aerodynamic load and pressure field measurements on turbines by non-intrusive piv. *Renew Energy* 63:181–193
- Wagner H (1925) Über die entstehung des dynamischen auftriebes von tragflügeln. *ZAMM J Appl Math Mech* 5(1):17–35
- Wang C, Eldredge JD (2013) Low-order phenomenological modeling of leading-edge vortex formation. *Theoret Comput Fluid Dyn* 27(5):577–598
- Widmann A, Tropea C (2015) Parameters influencing vortex growth and detachment on unsteady aerodynamic profiles. *J Fluid Mech* 773:432–459
- Wieneke B (2015) Piv uncertainty quantification from correlation statistics. *Meas Sci Technol* 26(7):074002
- Willert CE, Gharib M (1991) Digital particle image velocimetry. *Exp Fluids* 10(4):181–193
- Wu J-Z, Lu X-Y, Zhuang L-X (2007a) Integral force acting on a body due to local flow structures. *J Fluid Mech* 576:265–286
- Wu J-Z, Ma H-Y, Zhou M-D (2007b) Vorticity and vortex dynamics. Springer Science & Business Media, Berlin
- Xia X, Mohseni K (2013) Lift evaluation of a two-dimensional pitching flat plate. *Phys Fluids* 25(9):091901
- Zhu Q (2011) Optimal frequency for flow energy harvesting of a flapping foil. *J Fluid Mech* 675:495–517

Publisher's Note Springer Nature remains neutral with regard to jurisdictional claims in published maps and institutional affiliations.